Discrete microfluidics based on aluminum nitride surface acoustic wave devices

Discrete microfluidics based on aluminum nitride surface acoustic wave devices

J. Zhou, H. F. Pang, L. Garcia-Gancedo, E. Iborra, M. Clement, M. De Miguel-Ramos, H. Jin, J. K. Luo, S. Smith, S. R. Dong, et al.

Microfluidics and Nanofluidics

ISSN 1613-4982
Volume 18
Number 4

Microfluid Nanofluid (2015) 18:537-548
DOI 10.1007/s10404-014-1456-1

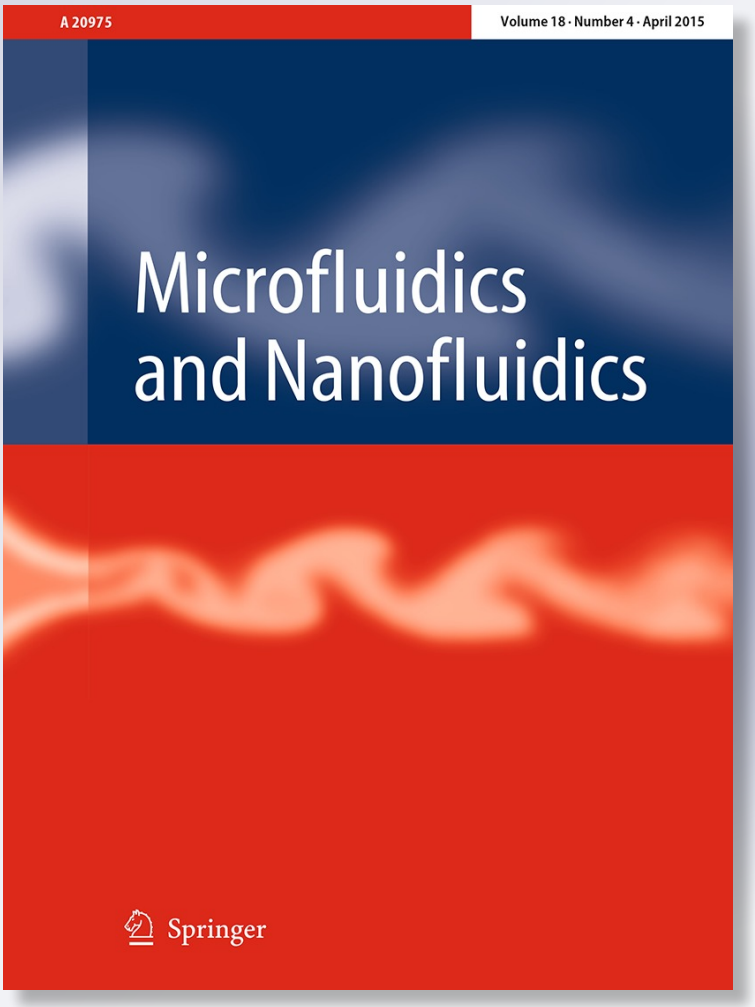

Springer

Microfluid Nanofluid (2015) 18:537–548
DOI 10.1007/s10404-014-1456-1

RESEARCH PAPER

Discrete microfluidics based on aluminum nitride surface acoustic wave devices

J. Zhou · H. F. Pang · L. Garcia-Gancedo · E. Iborra · M. Clement · M. De Miguel-Ramos · H. Jin · J. K. Luo · S. Smith · S. R. Dong · D. M. Wang · Y. Q. Fu

Received: 15 January 2014 / Accepted: 1 July 2014 / Published online: 14 July 2014

Abstract To date, most surface acoustic wave (SAW) devices have been made from bulk piezoelectric materials, such as quartz, lithium niobate or lithium tantalite. These bulk materials are brittle, less easily integrated with electronics for control and signal processing, and difficult to realize multiple wave modes or apply complex electrode designs. Using thin film SAWs makes it convenient to integrate microelectronics and multiple sensing or microfluidics techniques into a lab-on-a-chip with low cost and multi-functions on various substrates (silicon, glass or polymer). In the work, aluminum nitride (AlN)-based SAW devices were fabricated and characterized for discrete microfluidic (or droplet based) applications. AlN films with a highly *c*-axis texture were deposited on silicon substrates using a magnetron sputtering system. The fabricated AlN/Si SAW devices had a Rayleigh wave mode at a frequency of 80.3 MHz (with an electromechanical coupling coefficient k^2 of 0.24 % and phase velocity v_p of 5,139 m/s) and a higher-frequency-guided wave mode at 157.3 MHz (with a k^2 value of 0.22 % and v_p of 10,067 m/s). Both modes present a large out of band rejection of $\sim$15 dB and were successfully applied for microfluidic manipulation of liquid droplets, including internal streaming, pumping and jetting/nebulization, and their performance differences for microfluidic functions were discussed. A detailed investigation of the influences of droplet size (ranging from 3 to 15 μL) and RF input power (0.25–68 W) on microdroplet behavior has been conducted. Results showed that pumping and jetting velocities were increased with an increase of RF power or a decrease in droplet size.

Keywords Surface acoustic wave · SAW · AlN film · Microfluidic · Streaming

J. Zhou and H. F. Pang contributed equally to this work.

J. Zhou · H. Jin · J. K. Luo · S. R. Dong · D. M. Wang
Department of Information Science and Electronic Engineering, Zhejiang University, Hangzhou 310027, China

J. Zhou · H. F. Pang · Y. Q. Fu (✉)
Thin Film Centre, Scottish Universities Physics Alliance (SUPA), University of the West of Scotland, Paisley PA1 2BE, UK
e-mail: richard.fu@uws.ac.uk

J. Zhou · S. Smith
Institute for Bioengineering, School of Engineering, The University of Edinburgh, Edinburgh EH9 3JF, UK

H. F. Pang
Department of Applied Physics, School of Science, Xi'an University of Science and Technology, Xi'an 710054, People's Republic of China

L. Garcia-Gancedo
Electrical Engineering Division, Department of Engineering, University of Cambridge, Cambridge CB3 0FA, UK

E. Iborra · M. Clement · M. De Miguel-Ramos
GMME-CEMDATIC, Escuela Técnica Superior de Ingenieros de Telecomunicación, Universidad Politécnica de Madrid, Madrid 28040, Spain

1 Introduction

Surface acoustic waves (SAWs) have been used for microfluidic applications, including streaming, pumping, jetting and nebulization as illustrated in Fig. 1 (Wixforth 2006; Yeo and Friend 2009, 2013; Friend and Yeo 2011; Tan et al. 2007, 2009; Li et al. 2012a; Fu et al. 2010a; Du et al. 2008, 2009; Franke 2009; Wixforth 2003; Ding 2013; Shilton et al. 2008). Microfluidic devices based on SAWs provide an efficient, reliable and controllable method to

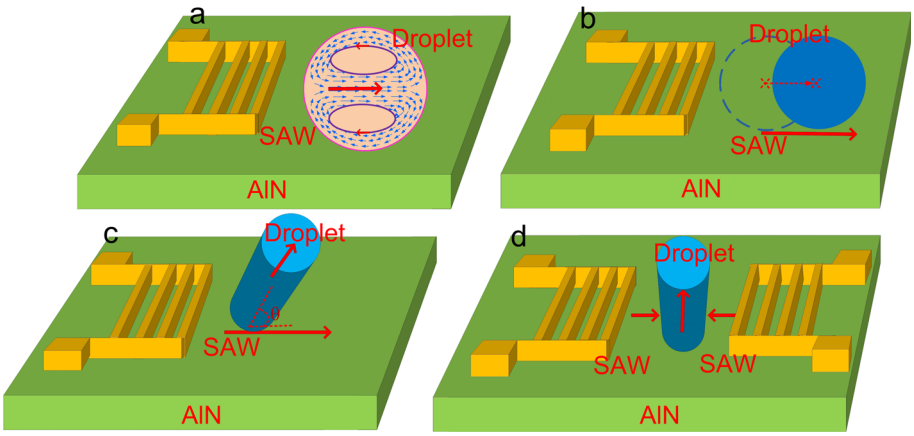

Fig. 1 Schematic illustrations of microfluidic functions of conventional SAW devices: **a** streaming; **b** pumping; **c** inclined jetting; **d** vertical jetting

modulate microfluidic actuation and manipulation, trap and sort cells and pattern microparticles (Franke et al. 2010; Jin et al. 2013; Shi et al. 2009; Guttenberg et al. 2005; Özgür et al. 2005; Fu et al. 2012a). Piezoelectric materials, either in bulk form (such as quartz, $LiNbO_3$ or $LiTaO_3$) or in thin film form (such as ZnO or AlN), have been reported to be well suited for the fabrication of SAW devices (Kovacs et al. 1990; Reboud et al. 2012; Li et al. 2012b). The bulk materials are generally brittle, less easily integrated with electronics for control and signal processing, and difficult to realize multiple wave modes or apply complex designed electrodes. Thin film materials present several distinct advantages over bulk materials in terms of device design flexibility, cost and easiness of fabrication and integration other electronic devices (Li et al. 2012a; Guttenberg et al. 2005; Garcia-Gancedo et al. 2012). Furthermore, thin film SAW devices could be made on flexible substrates such as metallic or polymer foils and plates for flexible SAW-based sensors, display and microfluidics devices (Jin et al. 2013).

In the past 10 years, many studies on microfluidic applications using ZnO-based SAW devices have been reported (Lee et al. 2006, 2007; Zhou et al. 2013a; Pang et al. 2013a). However, ZnO films present several issues (such as chemical instability when used in liquid environments) (Kim et al. 2006), making them less than ideal for their use in microfluidic applications. ZnO is also prone to form oxygen vacancies, thus increasing potential failure due to ionic conduction, acoustic losses and inter-diffusion upon metallization (Vanni et al. 2006; Pagán et al. 2009). Whereas, AlN films possess better chemical/thermal stabilities, higher phase velocity and dielectric strength than those of ZnO films (Iriarte et al. 2010; Cheng and Sun 2003; Jin et al. 2012). Owning to the rapid development of resonators and multiplexers for mobile phone applications, AlN films have already been used into industrial production and AlN-based device processing is becoming increasingly mature (Heinze et al. 2004). From this point of view, AlN film is a good candidate material to be used in both sensing and microfluidics, i.e., to form an integrated lab-on-a-chip (LOC) device (Wingqvist 2010). Similar to ZnO film, AlN film can be deposited by several techniques, among which reactive magnetron sputtering is the most commonly used one.

At present, there are many theoretical and experimental studies using AlN SAWs and film bulk acoustic wave resonators for sensing applications (Hou et al. 2012; Zhou et al. 2012; Fu et al. 2010b); however, little information is available on the microfluidic performance of the AlN-based SAW devices. This work demonstrates, for the first time, the microfluidic performance (including streaming, pumping, jetting and nebulization as illustrated in Fig. 1) of the AlN/Si SAW devices.

2 Experimental

AlN films of $\sim$4.7 μm thickness were deposited onto 4-inch (100)-oriented Si substrate using a pulsed-DC reactive magnetron sputtering process in an ultra-high vacuum system. The diameter of the high-purity (99.999 %) Al metallic target was $\sim$150 mm. Before AlN deposition, the substrates were heated to 400 °C with a base pressure of 1×10^{-8} Torr. The surface of the substrate was plasma-cleaned by means of a short bombardment (60 s) with Ar^+ ions from a bias RF glow discharge. The AlN films were then sputtered on top of the (100)-oriented high-resistive Si substrates using a gas mixture of $Ar:N_2$ (4:6), a total pressure of 1.9 mTorr, a pulsed-DC target power of 1.2 kW and a platen temperature of 400 °C. An RF bias power of 80 W, which leads to a DC polarization of −60 V, was applied to the substrates during the deposition in order to increase the adhesion of the film to the substrate and reduce the in-plane stress. The average deposition rate was estimated to be $\sim$640 nm min^{-1}. The crystal orientation of the AlN films was analyzed using X-ray diffraction (XRD, D5000, Siemens) with Cu-K_α

radiation ($\lambda = 1.5406$ Å). The film shows a strong (0002) orientation at 2θ value of 36.1°.

Cr/Au inter-digitized transducers (IDTs) were patterned using a conventional photolithography process. The IDTs have a spatial periodicity of 64 μm, 30 pairs of fingers and an aperture of 4.9 mm. The resonant characteristics of the devices were measured using an RF vector network analyzer (Agilent Technologies, E5061B).

For microfluidic tests, the SAW devices were surface-coated with a layer of CYTOP^{TM} (Asahi Glass Co. Ltd.) in order to enhance their surface hydrophobicity. The thickness of the CYTOP layer was around 300 nm, thin enough to minimize damping of the surface acoustic waves. For microfluidic testing, the devices were directly connected to a signal generator (Agilent Technologies N9310A) followed by a power amplifier (Amplifier research, 75A250). For signal generator, we used the dB units, and we fixed the gain 1 for amplifier. Before doing the experiments, we connected the signal generator to the power measurement machine and recorded the power value corresponding to the dB number for the generator. After that, we only needed to set the dB number and could know how much about the out power for the signal generator. All the system was carefully matched for negligible power reflection. The microfluidic behavior of de-ionized water droplets with various volumes ranging from 3 to 15 μL were recorded using a high-speed video camera (Vision Research, phantom V7.3) with a capture rate of 4,000 frames per second. The devices were mounted onto a bulk-aluminum test-holder during SAW jetting/nebulization testing in order to spread the possible generated heat, minimizing temperature variation effects. For some experiments where the stream velocity is measured, starch nanoparticles have been dispersed in the water to visualize the flow patterns or streamlines inside the droplets.

3 Results and discussions

3.1 Device characterization and FEM analysis

In telecommunication applications, the reflection coefficient is the ratio of the amplitude of the reflected wave to the amplitude of the incident wave while the transmission coefficient is the ratio of the amplitude of the complex transmitted wave to that of the incident wave at a discontinuity in the transmission line. In this work, typical experimental reflection (S_{11}) and transmission (S_{21}) signals of the AlN/Si SAW devices are shown in Fig. 2. The devices exhibit two clear transmission bands centered at 80.3 and 157.3 MHz, respectively. Both bands have a strong side-lobe suppression of ~15 dB. The phase velocity (v_p) of the SAW devices was determined by:

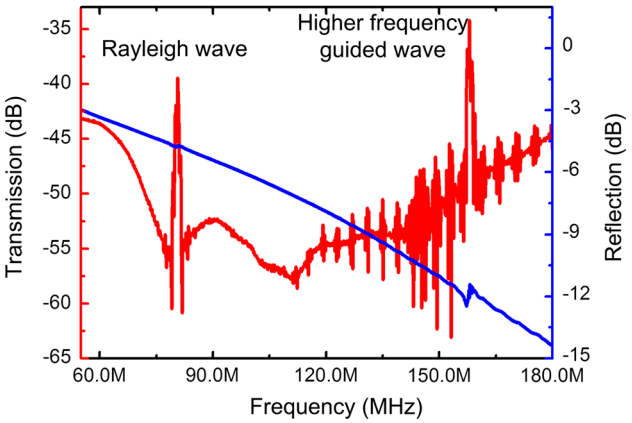

Fig. 2 Experimental transmission (S_{21}) (in *red*) and reflection (S_{11}) (in *blue*) signals of a typical AlN SAW device

$$v_p = \lambda f_0 \quad (1)$$

where λ is the wavelength of the SAW device, 64 μm, and f_0 is the measured resonant frequency. The corresponding velocity of the first peak was calculated to be about 5,139 m/s, which is attributed to the conventional Rayleigh wave mode. The second band is at 157.3 MHz, which gives a calculated propagating velocity of 10,067 m/s. It is associated with a higher-frequency-guided wave mode, which is propagating through interface between AlN films and substrate. There are significant spurious waves around the main peak of this guided wave, probably due to multiple reflections of skimming bulk waves generated at the input IDT on the AlN/Si interface, and detected at the output IDT (Lewis 1972).

For this layered structure, the phase velocity of the SAW device is influenced by the properties of both the piezoelectric layer and the substrate. The phase velocity for the Rayleigh wave in an ideal (0002) AlN layer is ~6,000 m/s (Iriarte et al. 2010), which is higher than that of Si (4,680 m/s) (Du et al. 2008). The second peak is not the Sezawa mode, which is commonly observed in a ZnO/Si or AlN/diamond SAW devices (Fu et al. 2010a; Du et al. 2008, 2009). This is because for the Sezawa mode, the velocity of piezoelectric layer is generally smaller than that of the substrate, whereas in this work, the velocity of the AlN layer is higher than the substrate of (100) Si.

In order to verify the vibration mechanisms of the AlN/Si SAWs, we have performed simulations of the various wave modes using the finite element analysis (FEA). The FEA has been conducted using the commercial COMSOL 3.5 software in a two-dimensional (2D) piezo plane strain mode to evaluate the SAW propagation properties, such as resonant frequency and wave modes of the AlN/Si SAW devices. IDTs are periodic in nature, alternatively consisting of positive and negative potentials. Thus, one period of the electrode would be sufficient to illustrate the

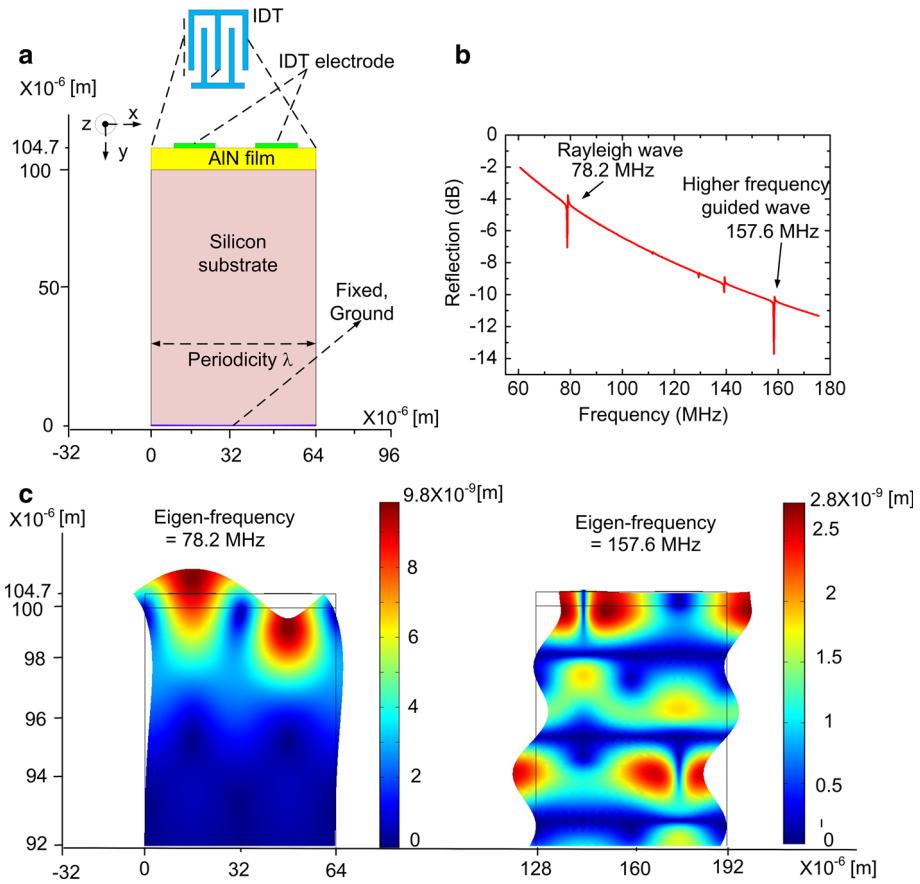

Fig. 3 **a** Geometry of a periodic cell in the simulation; **b** simulated reflection signal (S_{11}) of the AlN SAW device; **c** particle vibration and surface deformation of the two modes

performance of the SAW resonator (Zhou et al. 2013b; Chung and Phan 2010). The relationships among stress, strain, electric field and electric displacement field in the stress–charge of a piezoelectric crystal are given by the piezoelectric constructive as (Chung and Phan 2010):

$$T_{ij} = C^{E}_{ijkl} \cdot S_{kl} - e^{T}_{ijk} \cdot E_k \tag{2}$$

$$D_i = e_{ikl} \cdot S_{kl} - \varepsilon^{S}_{ij} \cdot E_j \tag{3}$$

where, T_{ij} represents the stress vector, C^{E}_{ijkl} is the elasticity matrix (N/m^2), e^{T}_{ijk} is the piezoelectric matrix(C/m^2), E_k is the electric field vector (V/m), ε^{S}_{ij} is the permittivity matrix (F/m), S_{kl} is the strain vector and D_i is the electrical displacement (C/m^2). The degrees of freedom (dependent variables) are the global displacements u_1, u_2 and u_3 in the global x_1, x_2 and x_3 directions. The electrical potential V can be obtained by solving the Newton and Maxwell equations related to Eqs. (1) and (2) (Chung and Phan 2010):

$$\sum_{ijk} C^{E}_{ijkl} \frac{\partial^2 u_l}{\partial x_j \partial x_k} + \sum_{jk} e_{kij} \frac{\partial^2 V}{\partial x_j \partial x_k} = \rho \frac{\partial^2 u_i}{\partial t^2} \tag{4}$$

$$\sum_{kl} e_{jkl} \frac{\partial^2 u_l}{\partial x_j \partial x_k} + \sum_{jk} \varepsilon^{S}_{jk} \frac{\partial^2 V}{\partial x_j \partial x_k} = 0 \tag{5}$$

for $i, j, k, l = 1, 2$ and 3.

In this work, a model of an AlN film with a thickness of 4.7 μm on a 100-μm-thick silicon substrate was used with a fixed bottom boundary condition. A free and zero charge/symmetry boundary condition was assigned to the top surface of the piezoelectric AlN layer. A polarization voltage value of 1 V was assigned to the gold electrode, which has a thickness of 70 nm, while the other gold electrode was assigned to be ground. The boundary between the AlN and Si was assigned to be free and continuous. The two sides of the AlN and Si substrate were assigned to be periodical boundary conditions. The material constants of the AlN film were obtained from Ref. Chung and Phan (2010). The simulation results are shown in Fig. 3. Clearly there are two large resonant peaks in the simulated frequency range which are corresponding to the two modes obtained from experimental work. Surface displacements, vibration and deformation of these two modes are shown in Fig. 3c, demonstrating that the first peak is corresponding to the Rayleigh wave mode, and the second mode is higher-frequency-guided wave mode.

The electromechanical coupling coefficients, k^2, of the two wave modes were calculated using the following formula based on the corresponding Smith et al. (1969):

$$k^2 = \frac{\pi}{4N} \left(\frac{G}{B} \right)_{f=f_o}, \tag{6}$$

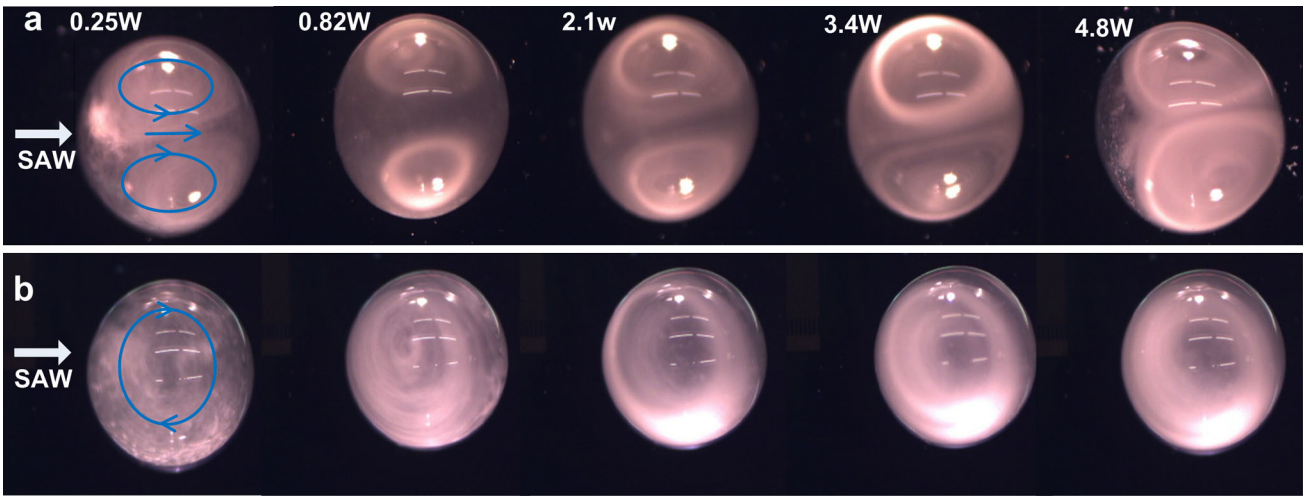

Fig. 4 **a** Effects of RF input power on acoustic streaming induced by AlN-based SAW device, showing a double vortex streaming pattern; **b** circulating streaming and concentration effects induced by AlN-based SAW off the central wave path with different RF powers

where N is the number of the finger pairs; G and B are the radiation conductance and susceptance at the central frequency, respectively. The value of k^2 for the Rayleigh and higher-frequency-guided wave modes for the AlN SAW device were found to be 0.24 and 0.22 %, respectively. These values are comparable to those reported elsewhere (Bu et al. 2004), but are significantly lower than those of the ZnO films (1.08 %) at a similar thickness and frequency (Pang et al. 2013a).

3.2 Streaming and concentration of Rayleigh mode

When a liquid droplet is located in the propagation path of a surface acoustic wave and an RF power level is applied to one of the IDTs at the center frequency of the transmission band (Rayleigh frequency), the propagating SAW interacts with the liquid and the acoustic energy couples into the liquid, inducing acoustic streaming (Jin et al. 2013). For the same droplet size, there are power boundaries for the various microfluidic phenomena of the liquid droplets, including internal streaming, pumping and ejection. Internal flowing/streaming occurs at a very low applied RF power, in the order of few mW. Higher power levels will result in an efficient droplet pumping/ejection.

When the applied RF power is larger than 0.25 W, the streaming trajectory of an 8 μL droplet shows a typical butterfly streaming pattern with a double vortex, as shown in Fig. 4a. This result is similar to others observed in ZnO-based SAW devices (Fu et al. 2012b; Alghane et al. 2011). The flow speed of the liquid in the droplet increases with the applied power. This feature can be used to control the mixing rate of a bioliquid in a biochemical reaction on a planar microfluidic device. The applied RF power also has an effect on the streaming velocity: When the applied RF power increases from 0.25 to 4.8 W, the streaming speed increases from 1.1 to 8.5 cm/s.

When a droplet is positioned off the central line of the wave path, the induced flow circulation due to asymmetric acoustic streaming rapidly establishes vortex patterns, as depicted in Fig. 4b, where some starch nanoparticles were added to the water to visualize the velocity field lines. The particle concentration is attributed to shear force inducing particle migration due to the gradient in the azimuthal streaming velocity in the droplet (Bourquin et al. 2010; Wilson et al. 2011). When the RF input power increases from 0.25 to 4.8 W, the time for concentration decreases from 8 to 0.5 s.

3.3 Pumping and jetting of Rayleigh mode

Figure 5 shows examples of pumping movement of a water droplet of 5 μL at an RF power of 22 W using the AlN SAW device. The droplet is deformed dramatically following the Rayleigh angle, and then pushed forward through sliding and rolling, in agreement with previous reports using ZnO-based devices (Fu et al. 2010a; Du et al. 2008). With the increase in the droplet size, the pumping speed decreases and the droplet moves in a crawling motion because of the increase in the area/volume ratio requires more acoustic energy to transport the droplet (Yeo and Friend 2009; Friend and Yeo 2011). The pumping speed increases significantly with the increase of RF power applied to the AlN SAW device.

Figure 6a–e shows significant deformation, pumping and jetting processes of the droplets with different volumes at an input power of 42 W. The measured top diameters of the droplets are 1.7, 2.1, 2.7, 3.2 and 3.8 mm, which correspond to volumes of 3, 5, 8, 10 and 15 μL, respectively.

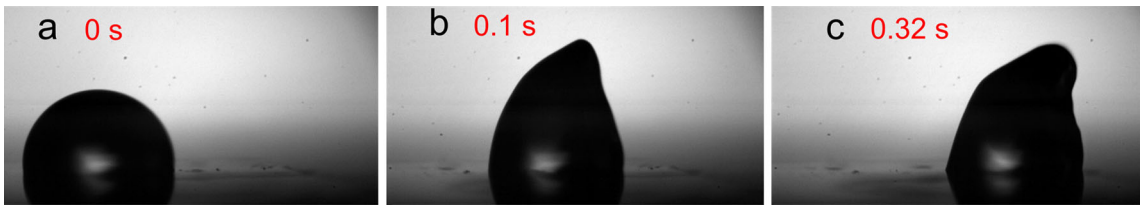

Fig. 5 Pumping of a 5 μL droplet at an input RF power of 22 W at various times after applying the SAW. **a** 0 s; **b** 0.1 s; **c** 0.32 s

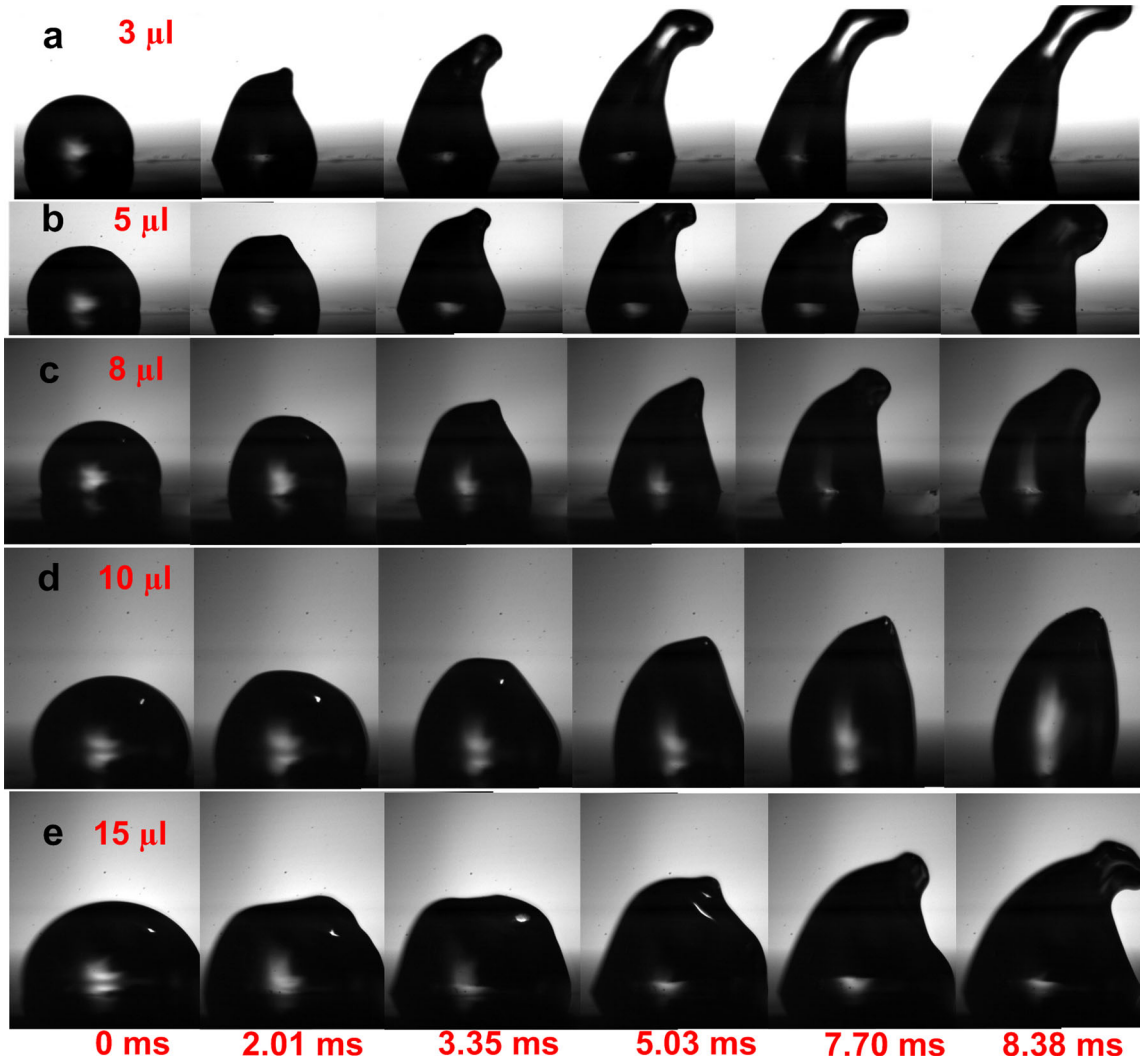

Fig. 6 High-speed jetting images of the **a** 3 μL, **b** 5 μL, **c** 8 μL, **d** 10 μL and **e** 15 μL droplet driven by the Rayleigh mode SAW (from left to right) at the power of 42 W

The effect of droplet size was investigated, as it could sensitively modulate the acoustic wave–liquid interaction during the acoustically induced droplet movement. The deformed shapes with asymmetric contact angles compared to the original sessile droplet indicate that the coupled SAWs formed different pressure gradients in those droplets. It is obvious that droplet of small size is easier to be ejected as they require less energy for ejection. For example, no significant jetting effect was observed in the droplets of sizes 8, 10 and 15 μL regardless of the RF power input (within the range investigated). Only streaming and pumping effects were observed in these droplets. When the droplet size decreases to 5 and 3 μL, ejection of the droplets can be clearly observed as shown in Fig. 6a, b.

Figure 7a, b shows the jetting images of an 8 μL droplet at different durations and different RF powers. With a

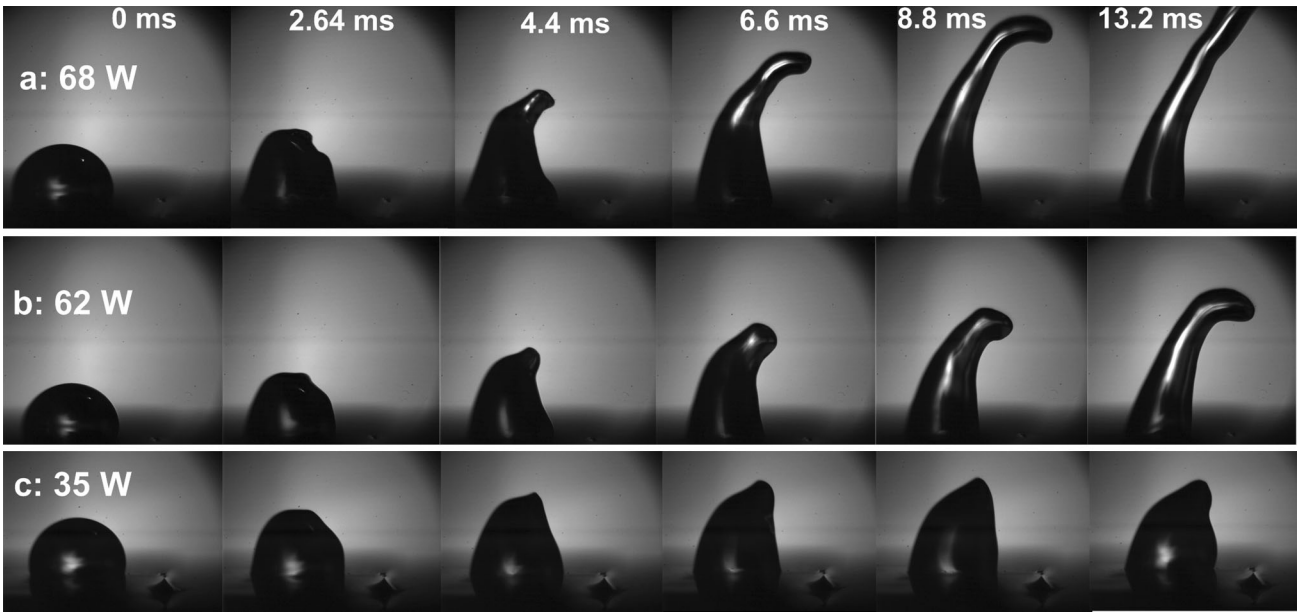

Fig. 7 High-speed jetting images of the 8 μL droplet driven by the Rayleigh mode SAW (from *left* to *right*) at the power of **a** 68 W; **b** 62 W; **c** 35 W

power of 68 W for 4.4 ms (Fig. 7a), or a power of 62 W for 6.6 ms (Fig. 7b), the droplet is ejected from surface initially into a broad beam, followed by formation of a coherent cylindrical liquid jetting beam, with a tilted angle of $\sim 72°$. The Rayleigh wave coupled into the droplet follows the Snell law of diffraction, in which the wave is refracted into the liquid at the Rayleigh angle, estimated using the following equation:

$$\theta_R = \sin^{-1}(V_{\text{water}}/V_{\text{AlN}}), \tag{7}$$

where V_{water} is the sound velocity into the droplet with a value of 1,495 m/s (Fu et al. 2012b) and V_{AlN} is the Rayleigh mode wave velocity with a value of 5,139 m/s, as determined above. The calculated Rayleigh angle is 16.9°. The jetting angle can be varied slightly around its complementary angle 73.1°, at different RF pulse durations due to the dissipation of the acoustic wave in the liquid. When the RF power is lower than 35 W, the RF power is not sufficient enough for the 8 μL droplet to be ejected and only pumping of the droplet was realized. Furthermore, with the increase on RF input power, the aspect ratio (length to diameter) of the ejected beam becomes larger, and the duration of the jetting is shorter as shown in Fig. 7a, b.

3.4 Effect of droplet size and RF power of Rayleigh mode

Figure 8 summarizes the microfluidic phenomena of the water droplets under different RF powers and different droplet sizes. For the same water droplet size, there are

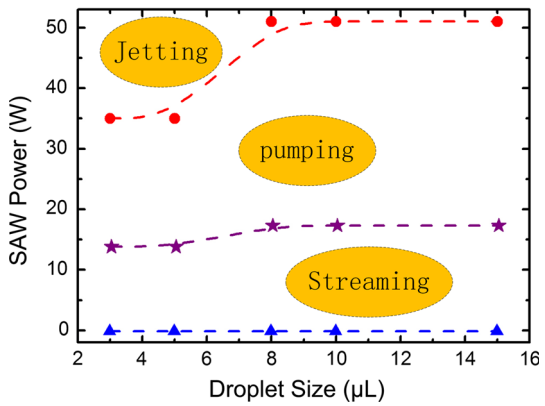

Fig. 8 Summary of streaming phenomena of the liquid droplets at different RF powers and different droplet sizes (the *lines* are guided to the eyes only)

power boundaries for the different microfluidic phenomena of the liquid droplets, including internal flowing/mixing, pumping and ejection. Internal flowing and streaming occur at the lowest RF power applied to the IDT of few mW. Higher power results in efficient droplet pumping/ejection depending on the droplet size. The jetting becomes difficult as the water droplet size increases, due to the reduced acoustic energy per unit volume feeding into the droplets as well as the increased mass of the droplet. Both contributions lead to a decrease in the pumping and ejection efficiency as the droplet size increases.

The estimated liquid velocities (including pumping and jetting) have been estimated from the analysis of the movie

frames for various droplet sizes at different RF powers, with the results shown in Fig. 9. With increased RF power, the velocity of all the droplets with different volumes increases. Furthermore, at the same RF power, with decreased droplet size, the acoustic wave propagation velocity increases.

Based on the analysis of a linearly fitted curve, an empirical relation between the pumping velocity (V_{pumping}) and jetting velocity (V_{jetting}) as a function of input power (P) can be obtained using the following equation:

$$\text{Log}_2\left(V_{\text{pumping}}\right) = aP + b \tag{8}$$

$$\text{Log}_2\left(V_{\text{jetting}}\right) = cP + d \tag{9}$$

where a, b, c and d are constants, which are mainly dependent on the droplet volume, wetting properties of the surface, liquid viscosity, electromechanical coupling coefficient and amplitude of the resonant signal of the acoustic wave. Table 1 lists the empirical results obtained for these constants for the AlN-based devices.

When the same input RF power was applied to both IDT transducers of the AlN SAW devices (i.e., forming a standing wave between the IDTs), the liquid droplet on the surface of the acoustic wave path was found to jump perpendicular from the substrate surface. Large acoustic energy dissipated into the droplet from both the opposite IDTs results in a large vertical inertial pressure in the droplet to overcome the sum of the weight and capillary force, resulting in a coherent cylindrical liquid beam, ejected vertically upwards. Figure 10 presents the images captured, showing vertical jetting and nebulization phenomena of a droplet of 3 μL induced by the surface acoustic waves with an RF power of 68 W. After applying a SAW power, the microscale capillary wave turbulences induced by the SAW have been observed using the high-speed camera, and there is a highly nonlinear balance between capillary forces and inertial forces, resulting in the droplet vibration, and pushed upwards from the two sides following the Rayleigh angle. The droplet is ejected from the sides based on the Rayleigh angle continuously and then reflected along the boundary of the liquid beams. Finally, the elongated jet suffered from the classical Rayleigh-Plateau instability (Tan et al. 2009) and broke up into small droplets as shown in the slides of Fig. 10a. Near to the end of the ejection process, nebulization of the remaining liquid droplets is also observed as shown in the last two frames of Fig. 10b.

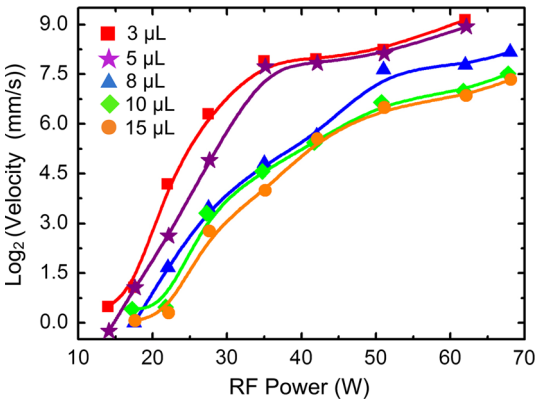

Fig. 9 Estimated velocities of pumping and jetting of water droplets as functions of droplet size and RF powers

Table 1 Experimental constants of the linearly fitting curve for pumping and jetting velocity

Droplet size (μL)	a	b	c	d
3	0.4594	−6.295	0.0465	6.1016
5	0.3788	−5.5784	0.0446	6.0441
8	0.2276	−3.4386	0.0289	6.1214
10	0.2262	−3.5401	0.0482	4.2795
15	0.2358	−4.0235	0.0477	4.2499

3.5 Microfluidic performance of the higher-frequency-guided wave mode

Figure 11a–c shows the streaming phenomena of the droplet of 8 μL with a power of 8.3 W for the higher guided wave mode at a frequency of 157.3 MHz. Similar to those from the fundamental Rayleigh wave modes, the higher guided wave could also generate typical SAW streaming patterns: both butterfly patterns and concentration of the liquid droplets as shown in Fig. 11. With an increase of the RF power, the streaming velocity increases. However, compared with those from the fundamental mode, the higher guided wave has a much weaker energy for deforming the droplet, and jetting could not be obtained with our power settings. This is mainly because the higher guided wave has a lower out-of-plane deformation of the AlN surface (as verified from FEA result in Fig. 3), which causes a lower momentum/energy transfer to the droplet in the vertical direction for the same RF excitation than the Rayleigh mode. Besides, higher-frequency waves could undergo of more energy dissipation, and thus, attenuation into the droplets becomes significant (Alghane et al. 2011).

Figure 11d–g shows the pumping phenomena of a droplet size of 3 μL, with a power of 68 W using the higher-frequency-guided wave mode. With such a high power, the fundamental frequency Rayleigh mode would eject the droplet (see Fig. 6), but the guided wave mode could only push the droplet forward with an estimated velocity of 20 mm/s. When the RF power is decreased from 68 to 62 W and then to 51 W, the pumping velocity decreases from 20 to 13 mm/s and to 6.6 mm/s,

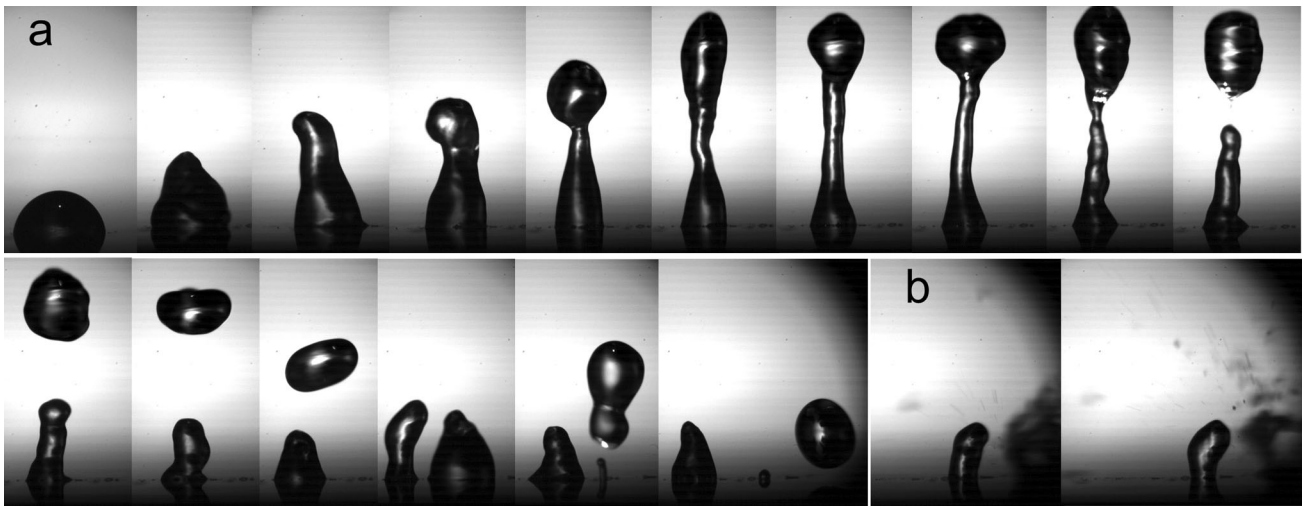

Fig. 10 High-speed images of vertical jetting and nebulization with an input RF power of 68 W applied to the two IDTs (the time spacing is 0.7 ms per frame)

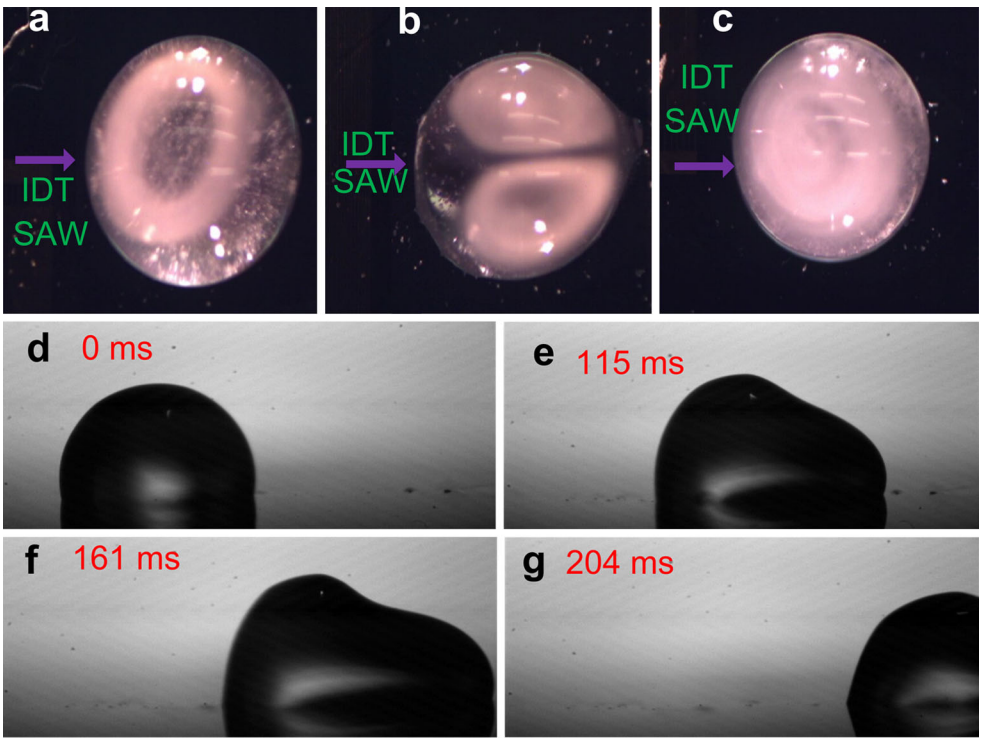

Fig. 11 Acoustic streaming and pumping of the droplet at frequency of 157.3 MHz: **a** streaming of droplet located *top side*; **b** *middle*; **c** *bottom side* of the IDTs with RF power of 8.3 W, as well as pumping effect for a droplet of 3 μL at an RF power of 68 W; **d** 0 s; **e** 115 ms; **f** 161 ms; **g** 204 ms

respectively. When the power is smaller than 51 W, the droplet could not be pumped forward. This critical power for pumping is much larger than that of fundamental mode (~14 W) as shown in Fig. 8. With the droplet size increased from 3 to 8 μL, the pumping velocity decreases from 20 to 8.4 mm/s at 68 W of RF power using the guided wave.

3.6 Comparison of AlN SAW performance with those of ZnO and $LiNbO_3$

Although all the microfluidic functions using AlN/Si SAW devices were demonstrated, it should be noticed that a much larger power was needed to realize similar microfluidic phenomena than using ZnO/Si based and $LiNbO_3$

based (Pang et al. 2013a; Fu et al. 2012b; Alghane et al. 2011).

$LiNbO_3$ has larger piezoelectric constant and better electromechanical coupling coefficient than thin film materials such as ZnO or AlN; therefore, it is easier to achieve microfluidic phenomena and smaller RF power needed to obtain the similar performance (Alghane et al. 2011). In addition, $LiNO_3$ bulk material has no thickness variation effects, the resonance frequency would be fixed when the wavelength is set as a value. For this reason, $LiNO_3$ SAW devices are popular for SAW microfluidic devices. However, $LiNO_3$ (and other piezoelectric bulk materials) is brittle and cannot be easily integrated with electronics for control and signal processing. Furthermore, the bulk material cannot form devices for flexible electronic application. Conversely, piezoelectric thin films are compatible with IC processing and have the potential to be used for flexible lab-on-a-chip (Jin et al. 2013; Zhou et al. 2013b).

Temperature variation of the AlN/Si SAW devices were measured as a function of time up to 1 min, using an infrared video camera (ThermaCAM^{TM} SC640) with the RF of 68 W. The temperature generally increased from 25 to 66 °C at the initial period of 0–5 s, but gradually reached a saturation value. The maximum temperature recorded was less than 70 °C. When the power was decreased to 22 W, the maximum temperature decreased to 55 °C. This values are comparable to the previous ZnO-based SAW results (Pang et al. 2013b). As opposed to the $LiNbO_3$-based SAW devices, cracking was never observed in the AlN/Si SAW devices to date, even when driving at high powers of 60–70 W for a few minutes and tens of thermal cycles. This can be attributed to the higher thermal conductivity and larger fracture strength of the Si substrate compared with those of the $LiNbO_3$.

A direct comparison for microfluidic performance between AlN and ZnO SAW devices is difficult as the optimized conditions for both piezoelectric films are dramatically different, and it is difficult to obtain two types of films with identical properties. Table 2 compares the measured data for selected AlN/Si SAW devices and ZnO/Si SAW devices, i.e., (a) 4.7-μm-thick AlN/Si SAW device with a frequency of 80.3 MHz, a coupling coefficient of 0.24 % and out of band rejection of 15 dB; and (b) 6.34-μm-thick ZnO SAW device with a frequency of 64.4 MHz, a coupling coefficient of 1.08 % and out of band rejection of 20 dB (Pang et al. 2013a; Fu et al. 2012b). Clearly, ZnO/Si SAW devices showed much lower critical powers for both pumping and jetting. The electromechanical coupling coefficients (K^2) of the ZnO/Si SAW devices were reported to be higher than those of the AlN/Si SAW devices (Pang et al. 2013a; Bu et al. 2004), because the piezoelectric constants (d_{33}) of ZnO are larger than those of AlN (Fu et al. 2010b; Trolier-Mckinstry and Muralt 2004). The higher k^2 of ZnO makes the ZnO-based SAW devices to exhibit better device performance in terms of transmission and reflection signals. In addition, lower power is needed to realize the microfluidic performance for ZnO-based SAW device compared with AlN-based SAW device.

Table 2 Critical values of the input power between the pumping and jetting phenomena based on the AlN/Si and ZnO/Si SAW devices, where the data (*) of the input power is cited from the Refs. Li et al. (2012b) and Smith et al. (1969)

Droplet size (μL)	Pumping power (W)		Jetting power (W)	
	ZnO*	AlN	ZnO*	AlN
3	3.2	14.0	13.0	27.5
5	3.2	14.0	12.8	27.5
10	4.0	17.5	16.0	51.0
15	6.0	17.5	21.0	51.0

The MEMS processing of AlN film is perfectly compatible with silicon semiconductor technology, whereas Zn, as a fast diffusing ion, is problematic. AlN is a large band gap (6 eV) material with a large resistivity, whereas ZnO is really a semiconductor (3.0 eV) with the inherent risks that off-stoichiometry might lead to doping (as, e.g., Zn interstitials) and thus to an increased conductivity. It is difficult to obtain ZnO with a high resistivity. The DC conductivity translates into a high dielectric loss at low frequencies, which is especially harmful for sensors and actuators working at frequencies below about 10 kHz.

With respect to ZnO, AlN has advantages of higher sound velocity, better electrical resistance, breakdown electric field and dielectric loss. AlN has much better mechanical properties (modulus and strength), resistance to humidity and better endurance to chemical etching. Moreover, the opposite temperature coefficients of delay of Si and AlN make these materials particularly suitable to implement thermally stable SAW devices. ZnO/Si SAW devices, however, is chemically reactive and sensitive to temperature, acids as well as water (Xu et al. 2003). In fact ZnO will dissolve in deionized water with a solubility of about 2 mg/l (Zhou et al. 2006). On the other hand, AlN is chemically inert and compatible with most of the microelectronic fabrication technologies. The AlN thin films have a much higher velocity and they are preferred to be used into high-frequency SAW biosensing devices (a few hundreds of MHz or GHz range) and film bulk acoustic wave devices (GHz and above). Furthermore, the coefficient of thermal expansion of AlN is much lower than that for ZnO, thus making AlN a better match to that of silicon and more suitable for integration with CMOS. In addition, if the devices were needed to be used at temperature above 400 °C, then AlN would be the preferred choice, by

considering good properties of the AlN film, i.e., high thermal conductivity and good electrical isolation.

The drawbacks using the AlN SAW devices compared with the ZnO ones is much larger intrinsic film stresses in the AlN thin films which may cause problems for device processing. Crystalline ZnO film is usually deposited at room temperature, whereas a good crystalline AlN films are usually deposited between 200 and 400 °C (which is the borderline for the CMOS circuitry). The vacuum conditions needed for the AlN deposition are far more demanding than the ZnO, which increases the tooling and maintenance costs. The processing parameters are quite strict for AlN film deposition compared to those of the ZnO films.

4 Conclusions

All the microfluidic functions including streaming, pumping, one-port jetting, vertical jetting and nebulization have been demonstrated using the AlN/Si SAW device, showing the potential to use the AlN-based SAW device as a planar microfluidic platform for lab-on-a-chip applications.

AlN film has been characterized on the Si substrate exhibiting highly *c*-axis orientation. The AlN-based SAW device shows two key propagation modes with an out of band rejection of 15 dB, which are the Rayleigh mode at 80.3 MHz (velocity of 5,139.2 m/s) and the higher guided wave mode at 157.3 MHz (velocity of 10,067 m/s), with the value of k^2 to be 0.24 and 0.22 %, respectively. FEM analysis found that the first mode is Rayleigh mode and the second mode is higher-frequency-guided wave mode. Both modes could be used for microfluidic applications, although the lower frequency (Rayleigh) mode has stronger microfluidic actuation effect.

Effects of RF power and droplet size on the microfluidic performance were systematically investigated. With the RF power increased or droplet size decreased, pumping and jetting velocity would increase for both the two modes. There are power boundaries among streaming, pumping and jetting. The droplet size has large effect on the power boundary, and with the droplet size increase, the power boundary would increase.

Acknowledgments The authors acknowledge support from the Royal Society-Research Grant (RG090609), the Scottish Sensing Systems Centre (S3C), Carnegie Trust Funding, Royal Academy of Engineering-Research Exchange with China and India, the EPSRC (Engineering and Physical Sciences Research Council) Engineering Instrument Pool for providing the high-speed video system (Photron XLR Express, VISION Research Phantom MIRO 4, infrared video camera ThermaCAM™ SC640), Cyrus Tang Center for Sensor Materials and Applications, Zhejiang University, the National Natural Science Foundation of China (No. 61171038, 61204124, 61274037), the Zhejiang Province Natural Science Fund Key Project (No. J20110271), the Fundamental Research Funds for the Central Universities (No. 2014QNA5002), the Zhejiang Provincial Natural Science Foundation of China (No. Z11101168) and the University Research Fund from Xi'an University of Science and Technology. Part of this work was funded by the European Commission through the 7th Framework Programme by the *RaptaDiag* project, the COST action IC1208 and by the Ministerio de Economía y Competitividad del Gobierno de España through project MAT2010-18933.

References

Alghane M, Fu YQ, Chen BX, Li Y, Desmulliez MPY, Walton AJ (2011) Streaming phenomena in microdroplets induced by Rayleigh surface acoustic wave. J Appl Phys 109:114901

Bourquin Y, Reboud J, Wilson R, Cooper JM (2010) Tuneable surface acoustic waves for fluid and particle manipulations on disposable chips. Lab Chip 10:1898–1901

Bu G, Ciplys D, Shur M, Schowalter LJ (2004) Electromechanical coupling coefficient for surface acoustic waves in single-crystal bulk aluminum nitride. Appl Phys Lett 84:4611–4613

Cheng H, Sun Y, Zhang JX, Zhang YB, Yuan S, Hing P (2003) AlN films deposited under various nitrogen concentrations by RF reactive sputtering. J Cryst Growth 24:46–54

Chung GS, Phan DT (2010) Finite element modeling of surface acoustic waves in piezoelectric thin films. J Korean Phys Soc 57:446–450

Ding XY, Li P, Lin S-CS, Stratton ZS, Nama N, Guo F, Slotcavage D, Mao XL, Shi JJ, Costanzo F, Huang TJ (2013) Surface acoustic wave microfluidics. Lab Chip 13:3626–3649

Du XY, Fu YQ, Tan SC, Luo JK et al (2008) ZnO film thickness effect on surface acoustic wave modes and acoustic streaming. Appl Phys Lett 93:094105

Du XY, Fu YQ, Tan SC, Luo JK, Flewitt AJ, Lee DS, Maeng S, Kim SH, Choi YJ, Park NM, Park J, Milne WI (2009) Microfluidic pumps employing surface acoustic waves generated in ZnO thin films. J Appl Phys 105:024508

Franke T, Abate AR, Weitz DA, Wixforth A (2009) Surface acoustic wave (SAW) directed droplet flow in microfluidics for PDMS devices. Lab Chip 9:2625–2627

Franke T, Braunmuller S, Schmid L, Wixforth A, Weitz DA (2010) Surface acoustic wave actuated cell sorting. Lab Chip 10:789–794

Friend JR, Yeo LY (2011) Microscale acoustofluidics: microfluidics driven via acoustics and ultrasonics. Rev Mod Phys 83:647–704

Fu YQ, Luo JK, Du X, Flewitt AJ, Li Y, Walton A, Milne WI (2010a) Recent developments on ZnO films for acoustic wave based biosensing and microfluidic applications: a review. Sens Actuat B 143:606–619

Fu YQ, Cherng JS, Luo J, Flewitt AJ, Walton AJ, Desmulliez M, Milne WI, Placido F (2010) Aluminium nitride thin film acoustic wave devices for Microfluidic and biosensing applications. In: Dissanayake DW (ed) Chapter 12, in acoustic waves. Rijeka, Croatia, Sciyo

Fu YQ, Li Y, Zhao C, Placido F, Walton AJ (2012a) Surface acoustic wave nebulization on nanocrystalline ZnO film. Appl Phys Lett 101:194101

Fu YQ, Garcia-Gancedo L, Pang HF, Porro S, Gu YW, Luo JK, Zu XT, Placido F, Wilson JIB, Flewitt AJ, Milne WI (2012b) Microfluidics based on ZnO/nanocrystalline diamond surface acoustic wave devices. Biomicrofluidics 6:02410

Garcia-Gancedo L, Pedros J, Zhao XB, Ashley GM, Flewitt AJ, Milne WI, Ford CJB, Lu JR, Luo JK (2012) Dual-mode thin film bulk acoustic wave resonators for parallel sensing of temperature and mass loading. Biosens Bioelectron 38:369–374

Guttenberg Z, Muller H, Habermuller H, Geisbauer A, Pipper J, Felbel J, Kielpinski M, Scriba J, Wixforth A (2005) Planar chip device for PCR and hybridization with surface acoustic wave pump. Lab Chip 5:308–317

Heinze H et al (2004) 3.8×3.8 mm^2 PCS-CDMA duplex incorporating thin film resonator technology. IEEE Ultrasonics Symposium, pp 1425–1428

Hou R, Hutson D, Kirk KJ, Fu YQ (2012) AlN thin film transducers for high temperature non-destructive testing applications. J Appl Phys 111:074510

Iriarte GF, Rodríguez JG, Calle F (2010) Synthesis of c-axis oriented AlN thin films on different substrates: a review. Mater Res Bull 45:1039–1045

Jin H, Zhou J, Dong SR, Feng B, Luo JK, Wang DM, Milne WI, Yang CY (2012) Deposition of c-axis orientation aluminum nitride films on flexible polymer substrates by reactive direct-current magnetron sputtering. Thin Solid Films 520:4863–4870

Jin H, Zhou J, He X, Wang W, Guo H, Dong S, Wang D, Xu Y, Geng J, Luo J, Milne WI (2013) Flexible surface acoustic wave resonators built on disposable plastic film for electronics and lab-on-a-chip applications. Sci Rep 3:2140

Kim I, Ku D, Ko J, Kim D, Lee K, Jeong J-H, Lee T, Cheong B, Baik YJ, Kim W (2006) Improvement of the thermal and chemical stability of Al doped ZnO films. J Electroceramics 17:241–245

Kovacs G, Anhorn M, Engan HE, Visintini G, Ruppel CCW (1990) Improved material constants for $LiNbO_3$ and $LiTaO_3$. Proc IEEE Ultrason Symp 1:435–438

Lee SH, Lee HJ, Oh D, Lee SW, Goto H, Buckmaster R, Yasukawa T, Tomokazu M, Soon-Ku H, Hyunchul K, Meoung-Whan C, Takafumi Y (2006) Control of the ZnO nanowires nucleation site using microfluidic channels. J Phys Chem B 110:3856–3859

Lee DS, Fu YQ, Maeng S, Du XY, Tan SC, Luo JK et al (2007) Integrated ZnO Surface acoustic wave microfluidic and biosensor system. IEEE international electron devices meeting, 10–12 Dec 2007, pp 851–854

Lewis MF (1972) New technique for the suppression of triple-transit signals in surface-acoustic-wave delay lines. Electron Lett 8:553–584

Li Y, Fu YQ, Brodie S, Mansuor A, Walton A (2012a) Enhanced microdroplet splitting, concentration, sensing and ejection by integration of electrowetting-on-dielectrics and surface acoustic wave. Biomicrofluidics 6:012812

Li Y, Fu YQ, Brodie SD, Alghane M, Walton AJ (2012b) Integrated microfluidics system using surface acoustic wave and electrowetting on dielectrics technology. Biomicrofluidics 6:012812

Özgür Ü, Alivov YaI, Liu C, Teke A, Reshchikov MA, Doğan S, Avrutin V, Cho S-J, Morkoç H (2005) A comprehensive review of ZnO materials and devices. J Appl Phys 98:041301

Pagán VR (2009) Aluminum nitride deposition/characterization and PMEMS/SAW device simulation/fabrication. Master thesis, West Virginia University

Pang HF, Fu YQ, Garcia-Gancedo L, Porro S, Luo JK, Placido F, Wilson JIB, Flewitt AJ, Milne WI, Zu XT (2013a) Enhancement of microfluidic efficiency with nanocrystalline diamond interlayer in the ZnO-based surface acoustic wave device. Microfluid Nanofluid 15(3):377–386

Pang HF, Garcia-Gancedo L, Fu YQ, Porro S, Gu YW, Luo JK, Zu XT, Placido F, Wilson JIB, Flewitt AJ, Milne WI (2013) Characterization of the surface acoustic wave devices based on ZnO/nanocrystalline diamond structures. Physica Status Solidi (a) 8:1575–1583

Reboud J, Bourquin Y, Wilson R, Pall GS, Jiwaji M, Pitt AR, Graham A, Waters AP, Coopera JM (2012) Shaping acoustic fields as a toolset for microfluidic manipulations in diagnostic technologies. PNAS 109:15162–15167

Shi J, Ahmed D, Mao X, Lin S-CS, Lawit A, Huang TJ (2009) Continuous particle separation in a microfluidic channel via standing surface acoustic waves (SSAW). Lab Chip 9:2890–2895

Shilton R, Tan MK, Yeo LY, Friend JR (2008) Particle concentration and mixing in microdrops driven by focused surface acoustic waves. J Appl Phys 104:014910

Smith WR, Gerard HM, Collins JH, Reeder TM, Shaw HJ (1969) Analysis of interdigital surface wave transducers by use of an equivalent circuit model. IEEE T Micro Theory 17(11):856–864

Tan MK, Friend JR, Yeo LY (2007) Microparticle collection and concentration via a miniature surface acoustic wave device. Lab Chip 7:618–625

Tan MK, Friend JR, Yeo LY (2009) Interfacial jetting phenomena induced by focused surface vibrations. Phys Rev Lett 103:024501

Trolier-Mckinstry S, Muralt P (2004) Thin film piezoelectrics for MEMS. J Electroceramics 12:7–17

Vanni L (2006) Aluminum nitride thin films for MEMS resonators: growth and characterization. Doctoral thesis, University of California, Santa Barbara

Wilson R, Reboud J, Bourquin Y, Neale SL, Zhang Y, Cooper JM (2011) Lab Chip. Phononic crystal structures for acoustically driven microfluidic manipulations 11:323–328

Wingqvist G (2010) AlN-based sputter-deposited shear mode thin film bulk acoustic resonator (FBAR) for biosensor applications—a review. Surf Coat Technol 205:1279–1286

Wixforth A (2003) Acoustically driven planar microfluidics. Superlattices Microstruct 33:389–396

Wixforth A (2006) Acoustically driven programmable microfluidics for biological and chemical applications. JALA 11:399–405

Xu T, Wu G, Zhang G, Hao Y (2003) The compatibility of ZnO piezoelectric film with micromachining process. Sens Actuat A 104:61–67

Yeo LY, Friend JR (2009) Ultrafast microfluidics using surface acoustic waves. Biomicrofluidics 33:012002

Yeo LY, Friend JR (2013) Surface acoustic wave microfluidics, annual review of fluid mechanics. doi:10.1146/annurev-fluid-010313-141418

Zhou J, Xu N, Wang ZL (2006) Dissolving behavior and stability of ZnO in biofluidics: a study on biodegradability of ZnO nanostructures. Adv Mater 18:2432–2435

Zhou J, Dong SR, Jin H, Feng B, Wang D (2012) Flexible surface acoustic wave device with AlN film on polymer substrate. J Control Sci Eng 2012:1–5

Zhou J, He XL, Wang WB, Zhu Q, Xuan WP, Jin H, Dong SR, Wang DM, Luo JK (2013a) Transparent surface acoustic wave devices on ZnO/glass using Al-Doped ZnO as the electrode. IEEE Electron Device Lett 34:1319–1321

Zhou J, He XL, Jin H, Wang WB, Feng B, Dong SR, Wang DM, Zou GY, Luo JK (2013b) Crystalline structure effect on the performance of flexible ZnO/polyimide surface acoustic wave devices. J Appl Phys 114:044502